Reaction-Path and Dual-Level Dynamics Calculations of the CH_3F + OH Reaction

J. Espinosa-García,*,† E. L. Coitiño,‡ A. González-Lafont,§ and J. M. Lluch§

Departamento de Química Física, Universidad de Extremadura, 06071 Badajoz, Spain, Laboratorio de Química Teórica y Computacional, Facultad de Ciencias, Universidad de la República, Montevideo, 11200, Uruguay, and Departament de Química, Universitat Autonoma de Barcelona, 08193 Bellaterra, Barcelona, Spain

Received: July 29, 1998; In Final Form: October 16, 1998

Using two approaches, reaction-path dynamics (which uses information on electronic structure energy and energy derivatives calculated ab initio along the minimum energy path) and dual-level dynamics (in which the reaction-path is calculated at a low level of theory, and stationary point information from a high level of theory is used to interpolate corrections to energy quantities, vibrational frequencies, and moments of inertia), the reaction-path for the CH_3F + OH reaction was traced. Qualitatively, both methods yield similar results, showing the usefulness of the more economical dual-level approach. The H_2O product may be vibrationally excited due to the nonadiabatic flow of energy between the reaction coordinate and the O−H bound mode. The rate coefficents were calculated for the temperature range 200−1000 K using the variational transition-state theory. The tunneling effect was included in the first approach using the small-curvature tunneling method, and in the second using the microcanonical optimized multidimensional tunneling method. Tunneling plays an important role in this reaction and the calculated rate coefficients show a more pronounced curvature in the Arrhenius plot than the experimental data.

1. Introduction

The study of the kinetics of halocarbons with the hydroxyl radical is very important for the knowledge of their combustion and of their role in atmospheric processes, particularly in the chemistry of stratospheric ozone. Experimentally, three techniques have been employed to study the rate coefficient of the reaction of fluoromethane (CH_3F) with the hydroxyl radical: discharge flow system,[1,2] flash-photolysis methods,[3,4] and relative rate measurements, which involve measurement of the fractional loss of the reactant compound compared to a reference compound, in the presence of OH.[5,6] In general, the flow measurements yield values lower than those obtained by flash-photolysis methods, and the differences are greater in the lower temperature range.

Unfortunately, there have been only a few studies of this reaction's temperature dependence,[2,4,5] and then only over a small temperature range (240−480 K). The first study was performed by Jeong and Kaufman[2] in the range 292−480 K, finding a small curvature in the Arrhenius plot. In 1985, Atkinson[7] compiled the earlier rate coefficients and recommended the expression

$$k = 5.51 \times 10^{-18}\, T^2 \exp(-1005 \pm 168/T)$$

$$\text{cm}^3\ \text{molecule}^{-1}\ \text{s}^{-1}$$

with an estimated uncertainty of ±30% at 298 K. Schmoltner et al. [4] studied this reaction in the range 243−373 K, and several different OH sources were used: H_2O, HONO, H_2O_2, and HNO_3. They found that the values at 298 K and above were essentially independent of the OH source; however, significant differences were observed between the results obtained using different sources at lower temperatures. The data were presented using an Arrhenius plot, and the plotted curve exhibited no curvature. Finally, Hsu and DeMore[5] studied the relative rates in the range 283−403 K, and again no curvature was found in the Arrhenius plot. DeMore[6] fits the results to

$$k = 4.4 \times 10^{-12} \exp(-1655/T)\ \text{cm}^3\ \text{molecule}^{-1}\ \text{s}^{-1}$$

with an estimated uncertainty of 10% at 298 K.

The above experimental disagreement concerning the curvature of the Arrhenius plot is probably simply a result of the small temperature range studied (240−480 K). However, this reaction presents a heavy−light−heavy (HLH) mass combination, which is a good candidate to present a large tunneling effect at low temperatures and, therefore, curvature in the Arrhenius plot. Obviously, this effect will become more patent when a larger range of temperatures is analyzed.

The large amount of experimental work contrasts with the paucity of theoretical studies, which have been limited to rate-coefficient calculations using conventional transition-state theory (TST). Thus, Jeong and Kaufman[8] carried out calculations using the conventional TST, and estimated the tunneling factors by the Wigner and the Eckart methods, which are known to underestimate this effect. Cohen and Benson[9] also used TST, but did not include the tunneling effect in the calculation.

To perform the dynamic and kinetic study of the title reaction, we decided to first compare two different approaches to calculating the necessary initial information concerning the potential energy surface (PES).

In the first approach, we used ab initio electronic structure information only in the region along the reaction-path,[10−12] which is usually referred to as a "direct dynamics" method,[11] and hereafter we shall call it the "reaction-path approach". This

* Author to whom correspondence should be addressed.
† Universidad de Extremadura.
‡ Universidad de la República.
§ Universitat Autonoma de Barcelona.

10.1021/jp9832138 CCC: $15.00
Published on Web 12/04/1998

method describes a chemical reaction by using ab initio information (energies, gradients, and Hessians) only in the region of configuration space along the reaction-path and has presented satisfactory results for some hydrogen abstraction reactions.[10,11,13−19] However, it has two major limitations: high computational cost, and the fact that the influence of the PESs large curvature on the tunneling effect cannot be taken into account. This last effect is especially important in reactions with a heavy−light−heavy (HLH) mass combination, such as the title reaction.

In the second approach, we used the "dual-level" methodology.[20−22] A "higher-level" is used at a few selected points, normally just the stationary points: reactants, products, and saddle point; and a "lower-level" is used at a large number of geometries to generate a wider PES representation. This permits the description of the wide reaction-swath[12] of geometries accessed by tunneling paths when the reaction-path curvature is large. To reduce the computational cost, we use semiempirical molecular orbital theory as the "lower-level". The dynamical calculations are carried out at this "lower-level", but the energies and frequencies are corrected by interpolated corrections (IC)[20] in order to obtain "higher-level" accuracy.

To obtain kinetic information we perform variational transition-state theory (VTST) calculations with the inclusion of multidimensional tunneling effects.

2. Methods

2.1. Dual-Level Approach. *Lower-Level Electronic Structure Calculations.* The semiempirical molecular orbital theory has been traditionally used as an economical alternative for theoretical electronic structure calculations. In this paper, we used the PM3 method.[23] This economical method permits the description of the wide reaction-swath region[12] of geometries accessed by tunneling paths when the reaction-path curvature is large, as in this case. To achieve a better representation of critical regions of the PES, in particular of the geometries and relative energies of the stationary points, an alternative is to develop a set of specific reaction parameters (SRP) for the semiempirical Hamiltonian.[24−26] In this reaction, however, the original parameters in the PM3 method already gave an adequate initial description of these stationary points (geometry and energy). Successive trials did not lead to any improvement. Thus, in this particular case, possibly due to a fortunate error cancellation, the original PM3 provides an adequate initial description as lower-level.

Higher-Level Electronic Structure Calculations. Geometries, energies, and first and second energy derivatives were calculated using the GAUSSIAN 94 system of programs.[27] In the first step, we calculated geometries, energies, and vibrational frequencies at all stationary points in second-order Møller−Plesset perturbation theory[28] (MP2) with full electron correlation. For the closed-shell systems, the MP2 wave function was based on the restricted Hartree−Fock (RHF) wave function and the 6-31G(d,p) basis set.[29] For the open-shell systems, the MP2 calculations were based on both an unrestricted Hartree−Fock (UHF) wave function[30,31] (UMP2, and the 6-31G(d,p) basis set) and a restricted open-shell Hartree−Fock (ROHF) wave function[32−34] (ROMP2, and the 6-311G(2d,2p) basis set). To avoid or, at least, to reduce the spin contamination of the UMP2 wave function, we used the spin projection operator as implemented in GAUSSIAN 94. The energy after the spin decontamination will be PUMP2 (projected UMP2). The expectation values of S^2 were about 0.75, indicating minor spin contamination. In these conditions, one may expect a similarity in behavior between the UMP2 and ROMP2 wave functions.

In a second step, to improve the energy description of the stationary points in the reaction-path, we made a single-point calculation at higher levels.

Level 1. We made a single-point calculation using the MP2/6-31G(d,p) optimized geometries with the single- and double-coupled cluster approach including a perturbative estimate of corrected triple excitations,[35] CCSD(T), using the 6-311++G-(2d,p) basis set. We denote this energy as

$$\text{CCSD(T)/6-311++G(2d,p)//(R-U)MP2/6-31G(d,p)}$$

where the double slash (X//Y) denotes geometry optimization at level Y and energies calculated at level X.

Level 2. Continuing with the CCSD(T) method, we increased the basis set using the augmented correlation-consistent polarized valence triple-ζ sets developed by Dunning et al.,[36] AUG-cc-pVTZ. We denote this energy as

$$\text{CCSD(T)/AUG-cc-pVTZ//(R-U)MP2/6-31G(d,p)}$$

Level 3. Finally, the scaling all correlation energy method (SAC)[37−40] was applied to correct the calculated energies of the reactants, products, and saddle point. In general, the SAC approach consists of scaling all the correlation energies, calculated as the difference between the Hartree−Fock (HF) and the post-Hartree−Fock (i.e. correlated) energies, by using a factor F, calculated as

$$F = \frac{D_e(\text{correlated}) - D_e(\text{HF})}{D_e(\text{exp}) - D_e(\text{HF})} \tag{1}$$

where D_e is the dissociation energy and "exp" denotes experimental. The SAC method has been successfully used to compensate the deficiences in the basis sets and in the treatment of electron correlation for several reactions.[41] We denote these methods by the name of the correlated level, for example, the SAC method with MP2 estimates of the correlation energy is called MP2-SAC. One advantage of these methods is that they can be used for the whole potential energy surface.[40] Thus, the scaled energy is

$$E_{SAC} = E_{HF} + \frac{E_{\text{correlated}} - E_{HF}}{F} \tag{2}$$

According to the standard notation[22] for dual-level dynamics, these calculations are labeled as

$$\text{high-level//(R-U)MP2/6-31G(d,p)///low-level}$$

This triple slash notation (X//Y///Z) denotes reaction-path construction at level Z, stationary point optimization and frequency calculation at level Y, and single-point energies calculated at higher-level X.

2.2. Reaction-Path Approach. Geometries, energies, and first and second energy derivatives were calculated using the GAUSSIAN 94 system of programs.[27] The stationary point geometries (reactants, products, and saddle point) are optimized using restricted (R) or unrestricted (U) second-order Møller−Plesset perturbation theory, MP2, with full electron correlation, using the 6-31G(d,p) basis set. Starting from the saddle-point geometry and going downhill to both the asymptotic reactant and product channels in mass-weighted Cartesian coordinates, we constructed the "intrinsic reaction coordinate" (IRC), or minimum energy path (MEP) at this level, with a gradient step size of 0.05 bohr amu$^{1/2}$, following the algorithm of González and Schlegel.[42,43] In addition, for 27 points along the MEP we

computed the gradients and the Hessians at this level. To improve the energy description of the stationary points on the reaction-path, we used the single-point calculations at the higher levels analyzed in the previous section.

2.3. Dynamics. In the dual-level approach, the reaction-path was computed using the Page−McIver method,[44] with a gradient step-size of 0.01 bohr and with the Hessian matrix being recalculated every 2 steps. The reaction-path was calculated from −2.0 bohr on the reactants side to +2.0 bohr on the products side. In this dual-level calculation, the interpolated corrections scheme[20] was applied to interpolate corrections to the frequencies at the MP2 level and energies to reproduce the higher-level behavior.

For both types of calculation, reaction-path and dual-level, s denotes the signed distance from the saddle point ($s = 0$) along the MEP in an isoinertial mass-scaled coordinate system, with $s > 0$ referring to the product side. An isoinertial coordinate system is any coordinate system in which the kinetic energy can be written in the form

$$\sum_{i=1}^{3N} p_i^2/(2\mu)$$

where μ is the common reduced mass for all degrees of freedom, p_i is a momentum component, and N is the number of atoms. In the rest of the work the units of s are bohr, and the reduced mass to scale the coordinates[45] is set to 1 amu. This has no effect on calculated observables, but it does affect the magnitude of s in plots used for interpretative purposes. In both cases, a generalized normal-mode analysis projecting out frequencies is performed,[46] which allows us to calculate both the vibrational partition function along the MEP and the vibrationally adiabatic ground-state potential energy curve

$$V_a^G(s) = V_{MEP}(s) + \epsilon_{int}^G(s) \quad (3)$$

where $V_{MEP}(s)$ is the classical energy along the MEP, and $\epsilon_{int}G(s)$ is the zero-point energy (ZPE) at s from the generalized normal-mode vibrations orthogonal to the reaction coordinate.

The rate coefficients are calculated using the canonical variational transition-state theory (CVT),[47] which locates the dividing surface between reactants and products along the MEP to minimize the generalized TST rate constants. CVT yields hybrid rate coefficients (i.e., classical reaction-path motion with other degrees of freedom quantized). To take into account the spin−orbit effects, we include correctly the $^2\Pi_{1/2}$ excited state of the OH radical in the reactant partition function (140 cm^{-1}).[48] Rotations are treated by the classical rigid rotor approximation, and vibrations are treated as quantum mechanical separable harmonic oscillators, with the generalized normal-modes[47] defined in redundant curvilinear coordinates.[49−51] The chosen curvilinear coordinates were all the possible bond lengths and bond angles. The advantage of curvilinear coordinates (nonlinear functions of Cartesian coordinates) over rectilinear ones (linear functions of Cartesian coordinates) is that in some cases the lowest bending frequencies had unphysical imaginary values over a wide range of the reaction coordinate using rectilinear coordinates, whereas these frequencies were real over the whole of the reaction-path using curvilinear coordinates. This behavior has been verified in several reactions.[49,52−55]

Finally, the tunneling factor is included. In the reaction-path approach we have information available only on the reaction-path, and the centrifugal-dominant small-curvature tunneling (SCT)[56] is used. In the dual-level approach we have available the wide reaction-swath region of geometries accessed by tunneling paths when the reaction-path curvature is large. Consequently, the microcanonical optimized multidimensional tunneling (μOMT)[57] is used, in which—at each energy—the transmission probability is taken as the maximum of two calculations, namely, a SCT calculation and a large-curvature ground-state approximation, version 3 (LCT),[47,56,58] allowing the system to reach all the accessible vibrational excited states into which tunneling proceeds.

The dual-level dynamical calculations were carried out using the MORATE code, version 7.8.1,[59] which is an interface between MOPAC 5.07mn[60] and POLYRATE 7.8.1.[61] The direct dynamics calculations were carried out using the POLYRATE 7.8.1 code.

TABLE 1: Reactant Properties for CH_3F + OH → CH_2F + H_2O

	CH_3F			OH		
	PM3[a]	MP2[b]	ROMP2[c]	PM3	MP2	ROMP2
geometry[d]						
R_{C-H}	1.092	1.087	1.084			
R_{C-F}	1.351	1.388	1.383			
R_{O-H}				0.937	0.971	0.964
<FCH	108.60	109.25	109.20			
frequencies[e]						
	3141	3241	3200	3987	3844	3839
	3087	3241	3200			
	3087	3135	3107			
	1533	1566	1535			
	1356	1566	1535			
	1356	1557	1531			
	1202	1230	1223			
	1016	1230	1223			
	1016	1115	1091			
ZPE [f]						
	24.0	25.6	25.3	5.7	5.5	5.5

[a] Semiempirical PM3 method. [b] (R-U)MP2 = FULL/6-31G(d,p). [c] ROMP2 = FULL/6-311G(2d,2p). [d] In angstroms and degrees; experimental values:[48] $CH_3F(C_{3v})$: 1.095 Å, 1.391 Å; $OH(C_{\infty v})$: 0.971 Å. [e] In cm^{-1}; experimental values:[48] CH_3F: 3006(2), 2965, 1467(2), 1464, 1182(2), 1049; ZPE = 24.00 kcal mol^{-1}; OH: 3735, ZPE = 5.3 kcal mol^{-1}. [f] Harmonic zero-point energy, in kcal mol^{-1}; the harmonic ZPE is one-half the sum of the frequencies for the bound modes.

3. Results and Discussion

3.1. Structures and Vibrational Frequencies. The reactant and product characteristics are listed in Tables 1 and 2, and the saddle-point characteristics in Table 3. The ab initio calculations (MP2 and ROMP2) reproduce well the experimental geometries of reactants and products, and show a similar behavior. The harmonic vibrational frequencies agree with experiments within 5% for both methods. The PM3 calculation underestimates the C−F and O−H bond lengths, due probably to the overestimate of the polarity in this method.

At the saddle point, the length of the bond that is broken (C−H′) increases by 12%, 11%, and 9%, at the PM3, MP2, and ROMP2 levels, respectively; and the length of the bond that is formed (O−H′) increases by 41%, 32%, and 36%, respectively. In all cases, the reaction of OH with CH_3F proceeds via an "early" transition state. This is the behavior expected from Hammond's postulate, since the reaction is very exothermic. At the three levels, the saddle point presents a "bent" structure, i.e., an angle C−H′−O different from 180°. The saddle point at each level was identified with one negative eigenvalue of the respective Hessian matrix and, therefore, one imaginary frequency. The PM3 and the ROMP2 methods present a similar imaginary frequency, greater in absolute value than the MP2

TABLE 2: Product Properties for $CH_3F + OH \rightarrow CH_2F + H_2O$[a]

	CH_2F			H_2O		
	PM3	MP2	ROMP2	PM3	MP2	ROMP2
geometry						
R_{C-H}	1.079	1.077	1.073			
R_{C-F}	1.315	1.348	1.339			
R_{O-H}				0.951	0.961	0.956
<FCH	116.94	114.32	114.75			
<HOH				107.70	103.84	103.36
frequencies						
	3165	3403	3371	3989	4030	3995
	3041	3244	3208	3868	3892	3882
	1566	1554	1520	1742	1684	1685
	1145	1219	1208			
	944	1214	1198			
	632	766	591			
ZPE						
	15.0	16.3	16.0	13.7	13.7	13.7

[a] As in Table I: experimental values:[48] H_2O (C_{2v}): 0.975 Å, 104.5°; 3755, 3651, 1595 cm^{-1}; ZPE = 12.9 kcal mol^{-1}.

TABLE 3: Saddle-Point Properties for $CH_3F + OH \rightarrow CH_2F + H_2O$[a]

	PM3	MP2	ROMP2
geometry			
R_{C-H}	1.088	1.085	1.082
R_{C-F}	1.340	1.376	1.371
R_{O-H}	0.941	0.971	0.965
$R_{C-H'}$	1.219	1.203	1.180
$R_{O-H'}$	1.329	1.285	1.312
<FCH	111.02	110.65	110.52
θ[b]	164.07	158.76	160.72
frequencies			
	3995	3841	3818
	3092	3285	3241
	3083	3180	3143
	1527	1636	1591
	1314	1546	1518
	1232	1324	1341
	1085	1307	1295
	1078	1202	1198
	981	1140	1120
	682	912	915
	607	713	755
	511	287	268
	253	210	191
	108	128	125
	2491i	2154i	2455i
ZPE			
	27.95	29.61	29.34

[a] As in Table II. [b] The angle θ is the angle between the C−H′ and O−H′ bonds, where H′ is the transferred proton.

result. The frequency of the saddle point of value 511 cm^{-1} at the PM3 level (287 and 268 cm^{-1} at MP2 and ROMP2 levels, respectively) corresponds to a large-amplitude rotation of the OH group around the reactive H′-O bond. This mode is treated as a hindered rotor in all calculations.

3.2. Energy Properties. The SAC method corrects the treatment of electron correlation at the molecular orbital correlated level with a finite basis set by the scaling factor F of eq 1. Table 4 lists the calculated and experimental bond dissociation energies for the C−H and O−H bonds and the factor F. The PMP2/6-31G(d,p) and CC/AUG-cc-pVTZ methods have the best balance with F values of 0.78/0.80 and 0.99/0.96 for the C−H and O−H bonds, respectively. This good balance achieved using the PMP2 approach for the present problem may be due to errors cancellation between the correlation energy, and the basis set.

TABLE 4: Bond Dissociation Energies, D_e (kcal mol^{-1}), and F Parameters for SAC Calculations

	C−H		O−H	
method[a]	D_e	F	D_e	F
A	102.6	0.78	117.2	0.80
B	105.4	0.87	123.1	0.94
C	105.8	0.90	119.1	0.84
D	108.0	0.99	123.6	0.96
expt[b]	108.1		125.3	

[a] A: PMP2/6-31G(d,p), B: ROMP2/6-311G(2d,2p); C: CCSD(T)/6-311++G(2d,p); D: CCSD(T)/AUG-cc-pVTZ. [b] Ref 48.

TABLE 5: Energy Properties (kcal mol^{-1}) for $CH_3F + OH \rightarrow CH_2F + H_2O$[a]

method	ΔV	ΔH_R	$\Delta V^{\ddagger}$	$\Delta H^{\ddagger}$
PM3	−24.1	−25.1	8.2	6.6
AM1	−31.1	−32.2	8.6	8.8
A[b]	−14.6	−15.4	7.5	5.7
A-SAC	−18.3	−19.1	3.9	2.1
B[b]	−17.6	−18.4	8.1	6.3
B−SAC	−19.5	−20.3	5.9	4.1
C[b]	−13.3	−14.1	7.3	5.5
C−SAC	−15.1	−15.9	4.9	3.1
D[b]	−15.6	−16.4	5.1	3.3
D-SAC	−16.1	−16.9	4.5	2.7
expt[c]		−18.8±7.5		

[a] ΔV: Classical reaction energy; ΔH_R: enthalpy of reaction at 298 K (ΔV + ΔTC); $\Delta V^{\ddagger}$: classical barrier height; $\Delta H^{\ddagger}$: enthalpy of activation at 298 K ($\Delta V^{\ddagger}$ + ΔTC). [b] As in Table IV; A: PMP2/6-31G(d,p), B: ROMP2/6-311G(2d,2p), C: CCSD(T)/6-311++G(2d,p), D: CCSD(T)/AUG-cc-pVTZ. [c] $\Delta H_R(\text{expt}) = \sum \Delta H_f = -18.8 \pm 7.5$ at 298 K; $\Delta H_f^{298}(CH_3F) = -56.0 \pm 6.9$ (ref 48), $\Delta H_f^{298}(OH) = 9.3 \pm 0.3$ (ref 48), $\Delta H_f^{298}(H_2O) = -57.7 \pm 0.0$ (ref 48), $\Delta H_f^{298}(CH_2F) = -6.9$ (ref 64), −7.8 (ref 65), −7.6 (ref 66).

Table 5 lists the energy properties at various levels. First, note that the experimental enthalpy of reaction presents a large error bar (±7.5 kcal mol^{-1}) due, mainly, to the uncertainties in the CH_3F enthalpy of formation. We have recently studied theoretically this compound with high-level calculations, and a value $\Delta H_f(298\ K) = -57.4 \pm 1.2$ kcal mol^{-1} was proposed.[62] With this large experimental error, all the theoretical calculations (except the Austin Model 1 method[63]) are within the experimental value, although the semiempirical PM3 method is at the lower limit. In general, the SAC methods present reasonable agreement with experiment.

With respect to the barrier height, a direct comparison of theory with experiment is not possible, but if one takes as reference the experimental activation energy at 298 K recommended by the JPL compilation,[67] 3.0 ± 0.6 kcal mol^{-1}, and takes into account that the reaction is bimolecular, one may obtain a first estimate for the experimental enthalpy of activation at 298 K: $\Delta H^{\ddagger} = 1.8 \pm 0.6$ kcal mol^{-1}. This is the value to be compared with the theoretical results in this paper. Note, however, that unfortunately an uncertainty of 1.3 kcal mol^{-1} in the activation energy means an uncertainty in the rate coefficient (298 K) of a factor of 10. The PM3, PMP2, ROMP2, and CC/6-311++G(2d,p) methods strongly overestimate this value. All SAC methods present a better behavior, especially PMP2-SAC and CC/AUG-cc-pVTZ-SAC.

3.3. Reaction-Path Analysis. Figure 1 shows the variation of the classical energy along the MEP for the MP2, PM3, and PM3 with interpolated corrections (PM3-IC) levels [the higher-level used will be analyzed below (section 3.4)]. In this case we use the original IC method,[20] where the correction ΔV to the lower-level $V_{MEP}(s)$ was done by fitting the corrections at reactants, products, and saddle point to an Eckart function, and

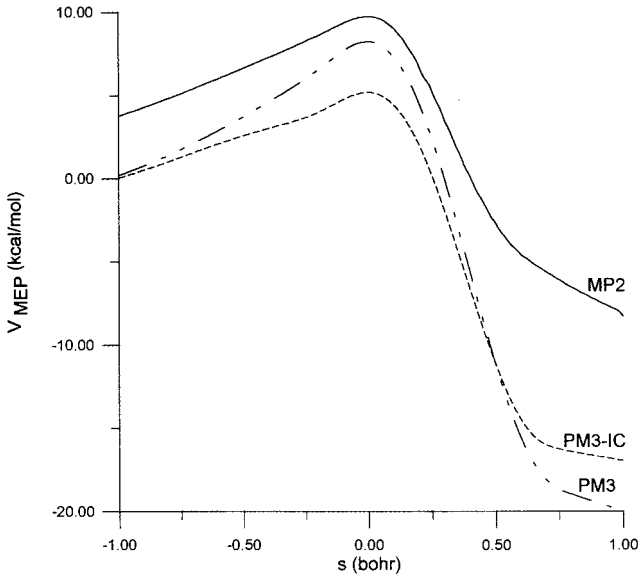

Figure 1. Classical potential energy curve (V_{MEP}) as a function of *s* at different computational levels: MP2, PM3, and PM3-IC (see text).

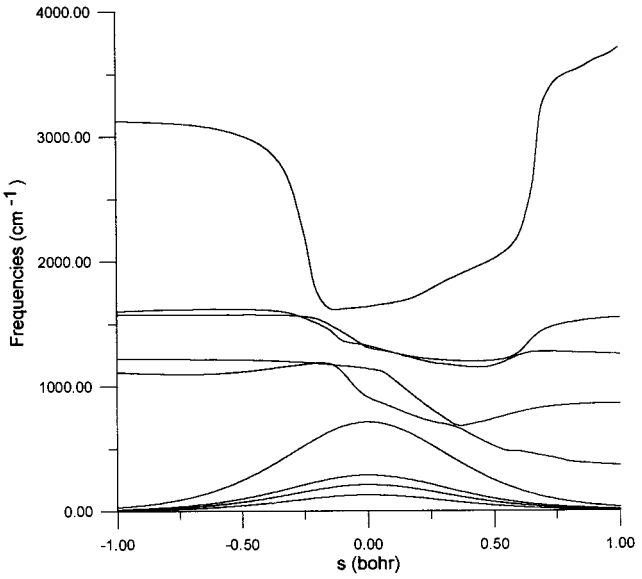

Figure 3. Generalized normal-mode vibrational frequencies plotted vs *s*.

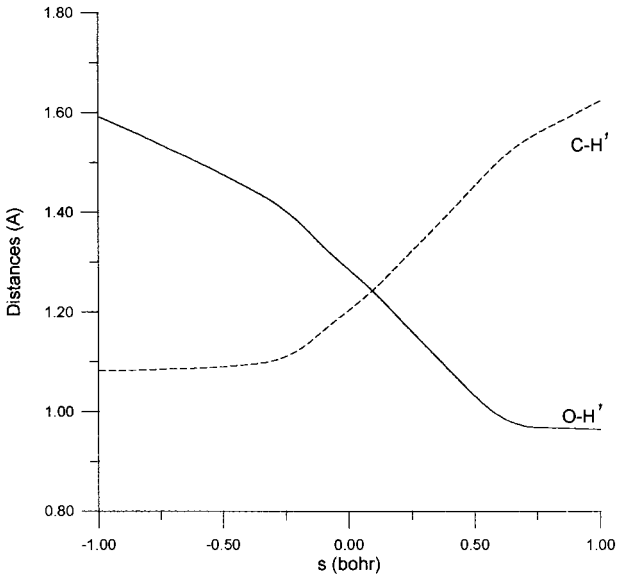

Figure 2. Bond distances between C and H′ and O and H′ as a function of *s*. Note that $s = 0$ corresponds to the saddle point.

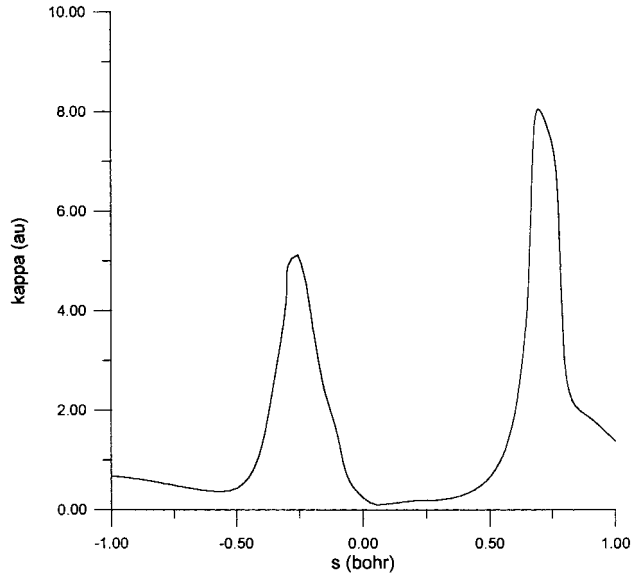

Figure 4. Curvature of the reaction-path (κ factor) as a function of *s*.

the MP2 imaginary frequency was not used in the fit. To test the sensitivity of this method, we performed a calculation with a more recent scheme of interpolated corrections, interpolated-corrections-logarithmic,[68] where the correction is approximated by the difference between two Eckart functions, one fitted to the lower-level V_{MEP}(s), and the other fitted to the higher-level energies for reactants, products, and saddle point, and the imaginary frequency at the saddle point is taken into account. In this case, where the differences between the lower-level and the higher-level are not important, we found no differences between both methods, in accordance with the suggestions of Truhlar et al.[55]

In the rest of this section, the reaction-path analysis is carried out only on the reaction-path approach, although it is interesting to note that the dynamic and kinetic conclusions were similar when the dual-level approach was used (not included here).

Figure 2 shows the variation of the distances of the broken (C−H′) and formed (O−H′) bonds as a function of *s*. As the reaction proceeds to products, the C−H′ bond remains practically constant until the reaction coordinate reaches about −0.25 bohr, where it starts changing almost linearly with *s*. A similar change is also observed for the forming bond, O−H′, at about +0.75 bohr. The points where these large changes take place show the beginning of the dissociation and the end of the formation of the C−H′ and O−H′ bonds, respectively, and their location is related to the larger changes in frequencies (Figure 3) and to the reaction-path curvature (Figure 4).

The vibrational frequencies with larger changes along the MEP are shown in Figure 3, where redundant curvilinear coordinates have been used. The mode related to the breaking (C−H′)/forming (O−H′) of the bonds shown in Figure 2 drops dramatically near the saddle point ($s = 0$) (reactive mode). This mode presents a widening of the vibrational well, an effect which has been found in other reactions with a small skew angle.[16,69] The fall and later rise of its frequency are located at approximately the same points where the C−H′ and O−H′ bonds are broken and formed, respectively (Figure 2). The four lowest vibrational frequencies along the reaction-path (transitional modes) correspond to the transformation of free rotations or free translations of the reactant or product limits into real vibrational motions in the global system. Their frequencies tend

asymptotically to zero at the reactant and product limits and reach their maximum in the saddle-point zone.

To test the sensitivity of using a curvilinear treatment of the vibrations, we performed similar calculations using rectilinear coordinates. We found that when the vibrations are treated by using rectilinear coordinates the frequencies of the four lowest modes became imaginary along the reaction-path. These imaginary frequencies are not due to ridges or bifurcations on the surface, but rather to the unphysicality of rectilinear coordinates.[49−51] This problem disappears when the vibrations are treated in curvilinear coordinates.

Further analyzing the reaction valley, the curvature term (κ) of the reaction-path as a function of s is plotted in Figure 4. There are two sharp peaks, one before and one after the saddle point, due to strong coupling with the C−H and the O−H stretch modes, respectively. This analysis shows that the reaction-path curvature must therefore be taken into account in order to calculate the tunneling effect.

At this point it is very instructive to consider the experimental thermochemistry of this reaction. Of the possible channels

$$CH_3F + OH \rightarrow CH_2F + H_2O \qquad \Delta H(298\ K) = -18.8\ \text{kcal mol}^{-1} \quad \text{(I)}$$

$$\rightarrow CH_3 + FOH \qquad \Delta H(298\ K) = +58.0\ \text{kcal mol}^{-1} \quad \text{(II)}$$

$$\rightarrow CH_3OH + F \qquad \Delta H(298\ K) = +17.4\ \text{kcal mol}^{-1} \quad \text{(III)}$$

channel (I) seems the thermochemically more favored. Note that the enthalpies of reaction (298 K) have been calculated as differences of experimental enthalpies of formation. The exothermicity of this reaction I leads to an "early" transition state and to reaction dynamics in which (i) the vibrational energy of the reactant molecule is ineffective in enhancing reactivity, and (ii) a substantial fraction of the energy of reaction appears as vibrational energy of products. The results of the coupling terms which form term κ in Figure 4 confirm this prediction. Thus, vibrational excitation of the H_2O product would be expected, whereas the effect of vibrationally exciting the C−H stretching mode of the CH_3F reactant would be ineffective in accelerating this reaction, due to the high vibrational quanta in the C−H bond. However, to the best of our knowledge, these effects have not been previously described in the literature.

The classical energy along the MEP, V_{MEP}, zero-point energy, ZPE, and the ground-state vibrationally adiabatic potential curve, V_a^G, eq 4, as a function of s are plotted in Figure 5. The V_a^G curve is wider, and the maximum is shifted to $s = -0.20$ bohr. This behavior is due to the ZPE, which presents a drop in a wide zone around the saddle point caused by the sharp drop of the reactive mode not compensated by the four transitional modes (Figure 3). Therefore, for this reaction, the entropy contribution dominates over the energy contribution at low temperatures.

Finally, to understand the zone where the reaction occurs we simultaneously analyze the internal parameter variation (Figure 2), the vibrational frequencies (Figure 3), the reaction-path curvature (Figure 4), and the energies (Figure 5). It can be seen that the breaking/forming bonds, the largest changes in the reactive mode, and the reaction-path curvature appear in a wide zone around the saddle point, from −0.3 to +0.7 bohr. The reason is clearly that these features are closely related.

3.4. Rate Coefficients. In the canonical version of VTST, CVT, the dividing surface is varied along the reaction-path to minimize the rate coefficients, obtaining the generalized transition state (GTS) at the value s^*.[47] Thermodynamically, the minimum rate coefficient criterion is equivalent to maximizing the generalized standard-state free energy of activation, $\Delta G^{GT,0}(T,s)$:

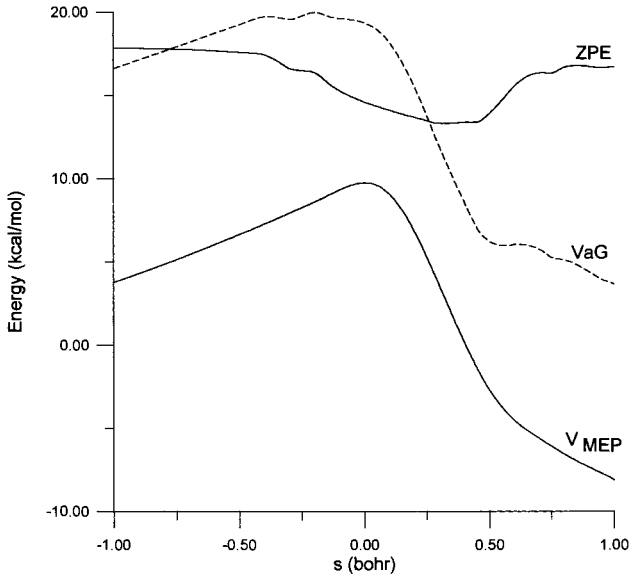

Figure 5. Classical potential energy curve (V_{MEP}), zero-point energy (ZPE) and vibrationally adiabatic potential energy curve (V_a^G) as a function of s.

$$k^{CVT}(s) = \sigma(k_B T/h)\, K^o \min(s) \exp[-\Delta G^{GT,0}(T,s)/kT] \qquad (5)$$

where σ is the reaction-path symmetry factor, k_B is the Boltzmann constant, h is the Planck constant, and K^o is the reciprocal of the standard-state concentration. Therefore, the effects of the potential energy, entropy, and temperature on the location of this GTS must be considered. Table 6 lists the rate coefficients for the CH_3F + OH reaction in the temperature range 200−1000 K for the two approaches studied in this paper: reaction-path and dual-level.

At this point we return to the discussion of the higher-level energy (section 3.2 and Table 5). A priori, as the SAC methods presented the best behavior, we choose as the highest-level classical energy barrier the average value of the four calculations: 4.8 kcal mol^{-1}. The rate coefficients using the reaction-path approach are strongly underestimated with respect to the experimental data, by a factor of from 25.2 to 8.2 when the temperature increases from 250 to 500 K. This behavior is due to a combination of the shape of the MP2 curve and the neglect of the curvature of the reaction-path (tunneling effect of large curvature). Using the second approach, dual-level, with the same classical energy barrier, 4.8 kcal mol^{-1}, and taking into account now the large-curvature tunneling effect, we found better agreement with experiment, although the rate coefficients are now overestimated by from 2.4 to 1.2 when the temperature increases from 250 to 500 K. To improve the agreement with experimental rate coefficients, we used the classical energy-barrier height as another semiempirical parameter. By trial and error, and using the highest temperature rates as a fitting criterion, we obtained a reasonable agreement with experiment in the common range of temperatures when the classical energy barrier is 5.2 kcal mol^{-1}. In this case too, we obtained an overestimate at low temperatures due to the tunneling effect. The activation energy at 298 K is 1.8 kcal mol^{-1}, therefore lower than the experimental value: 3.0 ± 0.6 kcal mol^{-1}.[67] This behavior is shown in Figure 6 for the dual-level approach, where

TABLE 6: Rate Coefficients (cm^3 $molecule^{-1}$ s^{-1}) for CH_3F + OH

			dual-level				
	reaction-path		$\Delta V^{\ddagger} = 4.8^a$		$\Delta V^{\ddagger} = 5.2^a$		
T (K)	CVT	CVT/SCT	CVT	CVT/μOMT	CVT/μOMT	expt[b]	expt[c]
200	6.50(−18)[d]	8.90(−17)	6.51(−17)	1.50(−14)	1.19(−14)		
250	7.55(−17)	3.83(−16)	6.50(−16)	2.28(−14)	1.77(−14)		9.65(−15)
300	4.05(−16)	1.25(−15)	3.16(−15)	3.73(−14)	2.86(−14)	1.74(−14)	2.30(−14)
350	1.39(−15)	3.22(−15)	1.02(−14)	6.15(−14)	4.72(−14)	3.82(−14)	4.26(−14)
400	3.62(−15)	6.93(−15)	2.53(−14)	9.90(−14)	7.65(−14)	7.15(−14)	6.78(−14)
450	7.81(−15)	1.31(−14)	5.27(−14)	1.53(−13)	1.20(−13)	1.20(−13)	
500	1.48(−14)	2.25(−14)	9.67(−14)	2.27(−13)	1.81(−13)	1.85(−13)	
600	4.04(−14)	5.43(−14)	2.53(−13)	4.53(−13)	3.70(−13)		
700	8.74(−14)	1.10(−13)	5.30(−13)	8.03(−13)	6.72(−13)		
1000	4.20(−13)	4.70(−13)	2.40(−12)	2.87(−12)	2.51(−12)		

[a] In kcal mol^{-1}. [b] $k(T) = 5.51 \times 10^{-18}$ T^2 exp(−1005/T) (ref 7). [c] $k(T) = 1.75 \times 10^{-12}$ exp(−1330/T) (ref 4). [d] 6.50(−18) stands for 6.50×10^{-18}.

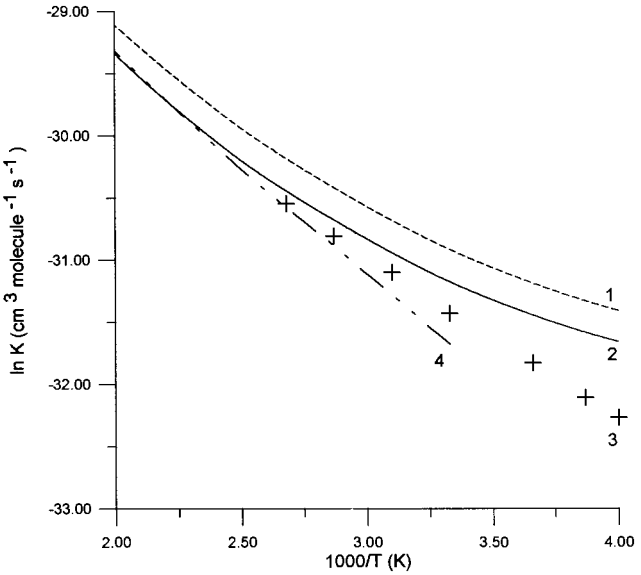

Figure 6. Arrhenius plot of ln k (cm^3 $molecule^{-1}$ s^{-1}) against the reciprocal of the temperature (K) in the range 250−500 K for the CH_3F + OH reaction. Line one (dashed): CVT/μOMT at the dual-level approach with $\Delta V^{\ddagger} = 4.8$ kcal mol^{-1}; Line two (solid): CVT/μOMT at the dual-level approach with $\Delta V^{\ddagger} = 5.2$ kcal mol^{-1}; number three (crosses): experimental values from ref 4; Line four (solid-dashed): experimental values from ref 7.

the Arrhenius plot is presented over the same temperature range experimentally determined (250−500 K). Clearly, our theoretical results show a greater curvature in the Arrhenius plot, especially at low temperatures, which is possibly due to an overestimation of the tunneling effect. At this point, a comment concerning the low-temperatures rate coefficients and the activation energy may be interesting. In this reaction a light atom (H) is transferred between two heavy atoms (C and O), and this heavy−light−heavy (HLH) mass combination is a good candidate to present a large tunneling effect at low temperatures so that one may expect the Arrhenius plot to be curved. Experimentally, Schmoltner et al.[4] and DeMore[6] fitted the results in Arrhenius form, i.e., no curvature was found, while Jeong and Kaufman[2] and Atkinson (compilation of data)[7] found a small curvature. For this HLH reaction it is surprising that no (or only small) curvature was found experimentally. This may be because the temperature dependence had been little studied, and the temperature range that had been analyzed was small. In fact, if we combine the results of Atkinson at high temperatures and Schmoltner et al. at low temperatures (see Figure 6), we find an appreciable curvature in the Arrhenius plot, in better accordance with our theoretical results. Clearly, more experimental studies of this reaction over a wider range of temperatures are necessary. Our previous experience with HLH reactions, NH_3 + OH,[16,22] CH_4 + Cl,[70] or CH_4 + O,[55] indicates that these reactions present curvature in their Arrhenius plots.

4. Conclusions

The present work has attempted to shed some light on the CH_3F + OH reaction, which is important in combustion and atmospheric chemistry, and presents theoretical and experimental challenges. Theoretically, the challenge is due to the flat potential energy surface. Experimentally, the curvature in the Arrhenius plot is still an open question. The present calculations show that tunneling plays an important role in this reaction and, therefore, a noticeable curvature can be expected in the Arrhenius plot.

With respect to the stationary points, the enthalpy of reaction and the barrier height strongly depend on the level of calculation and basis set. Thus, a priori, it is very difficult to choose a method as higher reference level. With respect to the reaction-path, first, it can be seen that the O−H stretching mode in the H_2O product strongly couples with the reaction coordinate in the exit channel and, therefore, an experimental vibrational excitation of this product can be expected. Second, the variation of the ZPE shows noticeable changes along the reaction-path, with a minimum in the saddle-point region. Because of the flattening of the reaction-path in the reactant channel, this ZPE change causes fairly marked variational effects, i.e., differences between the rate coeffcient calculated with the conventional and with the variational transition-state theories. An important conclusion is that the reaction-path and the dual-level approaches give a similar picture of this reaction. Thus, dual-level reaction-path calculations based on semiempirical molecular orbital calculations seem to be, because of their economy and the quality of their results that we tested with this reaction, a very promising tool for computing dynamical properties in reactions with halocarbons.

Acknowledgment. J.E.G. thanks the Dirección General de Investigación Científica y Técnica del Ministerio de Educación y Cultura (Spain) for partial support of this work (Project No. PB97-0368).

References and Notes

(1) Howard, C. J.; Evenson, K. M. *J. Chem. Phys.* **1976**, *64*, 197.
(2) Jeong, K. M.; Kaufman, F. *J. Phys. Chem.* **1982**, *86*, 1808.
(3) Nip, W. S.; Singleton, D. N.; Overnd, R.; Paraskevopoulos, G. *J. Phys. Chem.* **1979**, *83*, 2440.

(4) Schmoltner, A. M.; Talukdar, R. K.; Warren, R. F.; Mellouki, A.; Goldfarb, L.; Gierczak, T.; McKeen, S. A.; Ravishankara, A. R. *J. Phys. Chem.* **1993**, *97*, 8976.
(5) Hsu, K. J.; DeMore, W. B. *J. Phys. Chem.* **1995**, *99*, 1235.
(6) DeMore, W. B. *J. Phys. Chem.* **1996**, *100*, 5813.
(7) Atkinson, R. *Chem. Rev.* **1985**, *85*, 69.
(8) Jeong, K. M.; Kaufmann, F. *J. Phys. Chem.* **1982**, *86*, 1816.
(9) Cohen, N.; Benson, S. W. *J. Phys. Chem.* **1987**, *91*, 162.
(10) Doubleday, C.; McIver, J. W.; Page, M. *J. Phys. Chem.* **1988**, *92*, 4367.
(11) Baldridge, K. M.; Gordon, M. S.; Steckler, R.; Truhlar, D. G. *J. Phys. Chem.* **1989**, *93*, 5107.
(12) Truhlar, D. G.; Gordon, M. S. *Science* **1990**, *249*, 491.
(13) Garrett, B. C.; Koszykowski, M. L.; Melius, C. F.; Page, M. *J. Phys. Chem.* **1990**, *94*, 7095.
(14) Isaacson, A. D.; Wang, L.; Scheiner, S. *J. Phys. Chem.* **1993**, *97*, 1765.
(15) Espinosa-García; J.; Corchado, J. C. *J. Chem. Phys.* **1994**, *101*, 1333.
(16) Espinosa-García; J.; Corchado, J. C. *J. Chem. Phys.* **1994**, *101*, 8700.
(17) Corchado, J. C.; Espinosa-García, J. *J. Chem. Phys.* **1996**, *105*, 3152.
(18) Espinosa-García, J.; Corchado, J. C.; Truhlar, D. G. *J. Am. Chem. Soc.* **1997**, *119*, 9891.
(19) Villà, J.; González-Lafont, A.; Lluch, J. M.; Corchado, J. C.; Espinosa-García, J. *J. Chem. Phys.* **1997**, *107*, 7266.
(20) Hu, W. P.; Liu, Y. P.; Truhlar, D. G. *J. Chem. Faraday Trans.* **1994**, *90*, 1715.
(21) Truhlar, D. G. In *The Reaction Path in Chemistry: Current Approaches and Perspectives*; Hedrich, D., Ed.; Kluwer: Dordrecht, The Netherlands, 1995; p 229.
(22) Corchado, J. C.; Espinosa-García, J.; Hu, W. P.; Rossi, I.; Truhlar, D. G. *J. Phys. Chem.* **1995**, *99*, 687.
(23) Stewart, J. J. P. *J. Comput. Chem.* **1989**, *10*, 221.
(24) González-Lafont, A.; Truong, T. N.; Truhlar, D. G. *J. Phys. Chem.* **1991**, *95*, 4618.
(25) Viggiano, A. A.; Paschkewitz, J.; Morris, R. A.; Paulson, J. F.; González-Lafont, A.; Truhlar, D. G. *J. Am. Chem. Soc.* **1991**, *113*, 9404.
(26) Liu, Y. P.; Lu, D.h.; González-Lafont, A.; Truhlar, D. G.; Garrettt, B. C. *J. Am. Chem. Soc.* **1993**, *115*, 7806.
(27) Frisch, M. J.; Trucks, G. W.; Schlegel, H. B.; Gill, P. M. W.; Johnson, N. G.; Robb, M. A.; Cheeseman, J. R.; Keith, T.; Petersson, G. A.; Montgomery, J. A.; Raghavachari, K.; Al-Laham, M. A.; Zakrewski, V. G.; Ortiz, J. V.; Foresman, J. B.; Ciolowski, J.; Stefanov, B. B.; Nanayakkara, A.; Challacombe, M.; Pemg, C. Y.; Ayala, P. Y.; Chen, W.; Wong, M. W.; Andres, V.; Replogle, E. S.; Gompers, R.; Martin. R. L.; Fox, D. J.; Binkley, J. S.; Defrees, D. J.; Baker, J.; Stewart, J. J. P.; Head-Gordon, M.; González, C.; Pople, J. A. *GAUSSIAN 94*, Gaussian, Inc.: Pittsburgh, PA, 1995.
(28) Møller, C.; Plesset, M. S. *Phys. Rev.* **1934**, *46*, 618.
(29) Hariharan, P. C.; Pople, J. A. *Theor. Chim. Acta* **1973**, *28*, 213.
(30) Pople, J. A.; Nesbet, R. K. *J. Chem. Phys.* **1959**, *22*, 571.
(31) Bartlett, R. J.; Purvis, G. D. *Int. J. Quantum Chem.* **1978**, *14*, 561.
(32) McWeeny, R.; Diercksen, G. H. F. *J. Chem. Phys.* **1968**, *49*, 4852.
(33) Lauderdale, W. J.; Stanton, J. F.; Gauss, J.; Watts, J. D.; Bartlett, R. J. *Chem. Phys. Lett.* **1991**, *187*, 21.
(34) Lauderdale, W. J.; Stanton, J. F.; Gauss, J.; Watts, J. D.; Bartlett, R. J. *J. Chem. Phys.* **1992**, *97*, 6606.
(35) Bartlett, R. J. *J. Phys. Chem.* **1989**, *93*, 1697.
(36) Kendall, R. A.; Dunning, T. H.; Harrison, R. J. *J. Chem. Phys.* **1992**, *96*, 6796.
(37) Gordon, M. S.; Truhlar, D. G. *J. Am. Chem. Soc*. **1986**, *108*, 5412.
(38) Gordon, M. S.; Truhlar, D. G. *Int. J. Quantum Chem.* **1987**, *31*, 81.
(39) Gordon, M. S.; Nguyen, K. A.; Truhlar, D. G. *J. Phys. Chem.* **1989**, *93*, 7356.
(40) Rossi, I.; Truhlar, D. G. *Chem. Phys. Lett.* **1995**, *234*, 64.
(41) Corchado, J. C.; Truhlar, D. G. In *Combined Quantum Mechanical and Molecular Mechanical Methods*; Gao, J., Thomson, M. A., Eds.; Am. Chem. Soc. Symposium Series, and references therein. To be published.
(42) González, C.; Schelegel, H. B. *J. Phys. Chem.* **1989**, *90*, 2154.
(43) González, C.; Schlegel, H. B. *J. Phys. Chem.* **1990**, *94*, 5523.
(44) Page, M.; McIver, J. W. *J. Chem. Phys.* **1988**, *88*, 922.
(45) Isaacson, A. D.; Truhlar, D. G. *J. Chem. Phys.* **1982**, *76*, 1380.
(46) Miller, W. H.; Handy, N. C.; Adams, J. E. *J. Chem. Phys.* **1980**, *72*, 99.
(47) Truhlar, D. G.; Isaacson, A. D.; Garrett, B. C. In *Theory of Chemical Reaction Dynamics*; Baer, M., Ed.; CRC: Boca Raton, FL, 1985; Vol. 4.
(48) JANAF Thermochemical Tables, 3rd Ed.; Chase, M. W., Jr., Davies, C. A., Downey, J. R., Frurip, D. J., McDonald, R. A., Syverud, A. N., Eds.; National Standard Reference Data Series, Vol. 14, National Bureau of Standards, Washington, D. C., 1985.
(49) Jackels, C. F.; Gu, Z.; Truhlar, D. G. *J. Chem. Phys.* **1995**, *102*, 3188.
(50) Chuang, Y. Y.; Truhlar, D. G. *J. Phys. Chem.* **1997**, *101*, 3808.
(51) Chuang, Y. Y.; Truhlar, D. G. *J. Phys. Chem.* To be published.
(52) Natanson, G. A.; Garrett, B. C.; Truong, T. N.; Joseph, T.; Truhlar, D. G. *J. Chem. Phys.* **1991**, *94*, 7875.
(53) Espinosa-García, J.; Corchado, J. C. *J. Phys. Chem.* **1996**, *100*, 16561.
(54) Corchado, J. C.; Espinosa-García, J. *J. Chem. Phys.* **1997**, *106*, 4013.
(55) Corchado, J. C.; Espinosa-García, J.; Neto, O. R.; Chuang, Y. Y.; Truhlar, D. G. *J. Phys. Chem.* **1998**, *102*, 4899.
(56) Lu, D.h.; Truong, T. N.; Melissas, V. S.; Lynch, G. C.; Liu, Y. P.; Garrett, B. C.; Steckler, R.; Isaacson, A. D.; Rai, S. N.; Hancock, G. C.; Lauderdale, G. C.; Joseph, T.; Truhlar, D. G. *Comput. Phys. Commun.* **1992**, *71*, 235.
(57) Liu, Y. P.; Lu, D.h.; González-Lafont, A.; Truhlar, D. G.; Garrett, B. C. *J. Am. Chem. Soc.* **1993**, *115*, 7806.
(58) Truong, T. N.; Lu, D.h.; Lynch, G. C.; Liu, Y. P.; Melissas, V. S.; Stewart, J. J. P.; Steckler, R.; Garrett, B. C.; Isaacson, A. D.; González-Lafont, A.; Rai, S. N.; Hancock, G. C.; Joseph, T.; Truhlar, D. G. *Comput. Phys. Commun.* **1993**, *75*, 143.
(59) Chuang, Y. Y.; Fast, P. L.; Hu, W. P.; Lynch, G. C.; Liu, Y. P.; Truhlar, D. G. MORATE, version 7.8.1.; University of Minnesota, Minneapolis, MN, 1997.
(60) Stewart, J. J. P.; Rossi, I.; Hu, W. P.; Lynch, G. C.; Liu, Y. P.; Truhlar, D. G. MOPAC, version 5.0.7.mn; University of Minnesota, Minneapolis, MN, 1997.
(61) Corchado, J. C.; Chuang, Y. Y.; Fast, P. L.; Villà, J.; Coitiño, E. L.; Hu, W. P.; Liu, Y. P.; Lynch, G. C.; Nguyen, K.; Kackels, C. F.; Gu, M. Z.; Rossi, I.; Clayton, S.; Melissas, V.; Steckler, R.; Garrett, B. C.; Isaacson, A. D.; Truhlar, D. G. POLYRATE, version 7.8.1.; University of Minnesota, Minneapolis, MN, 1997.
(62) Espinosa-García, J. *Chem. Phys. Lett.* **1996**, *250*, 71.
(63) Dewar, M. J. S.; Zoebisch, E. G.; Healy, E. F.; Stewart, J. J. P. *J. Am. Chem. Soc.* **1985**, *107*, 3902.
(64) Cadman, P.; Kirk, A. W.; Trotman-Dickenson, A. F. *J. Chem. Soc. Faraday Trans. 1* **1976**, *72*, 996.
(65) McMillen, D. F.; Golden, D. M. *Annu. Rev. Phys. Chem.* **1982**, *33*, 493.
(66) Rodgers, A. S. *Int. J. Chem. Kinet.* **1983**, *15*, 569.
(67) DeMore, W. B.; Sander, S. P.; Golden, D. M.; Hapson, R. F.; Kurylo, M. J.; Howard, C. J.; Ravishankara, A. R.; Kolb, C. E.; Molina, M. *Journal of Chemical Kinetics and Photochemical Data for Use in Stratospheric Modelling*. JPL Publication 94-26, JPL: Pasadena, CA, 1994.
(68) Chuang, Y. Y.; Truhlar, D. G. *J. Phys. Chem* **1997**, *101*, 3808.
(69) Bondi, D. K.; Connor, J. N. L.; Garrett, B. C.; Truhlar, D. G. *J. Chem. Phys.* **1983**, *78*, 5981.
(70) Espinosa-García, J.; Corchado, J. C. *J. Chem. Phys.* **1996**, *105*, 3517.